Computational prediction of new magnetic materials

Saeed Rahmanian Koshkaki, Zahed Allahyari, Artem Oganov, Vladimir Solozhenko, Ilya Polovov, Alexander. Belozerov, Andrey Katanin, Vladimir Anisimov, Evgeny Tikhonov, Guang-Rui Qian, et al.

Computational prediction of new magnetic materials

Saeed Rahmanian Koshkaki[1,2,3,*,§], Zahed Allahyari[1,*†], Artem R. Oganov[1,‡], Vladimir L. Solozhenko[4], Ilya B. Polovov[5], Alexander. S. Belozerov[1,6], Andrey A. Katanin[2,6,1], Vladimir I. Anisimov[1,6,5], Evgeny V. Tikhonov[1,7], Guang-Rui Qian[7], Konstantin V. Maksimtsev[5], Andrey S. Mukhamadeev[5], Andrey V. Chukin[5], Aleksandr V. Korolev[6,5], Nikolay V. Mushnikov[6,5] Hao, Li[8,9,1]

[1]Skolkovo Institute of Science and Technology, 30 bldg. 1, Bolshoy blvd., Moscow 121205, Russia
[2]Moscow Institute of Physics and Technology, 9 Institutskiy lane, Dolgoprudny 141700, Russia
[3] Department of Physics, The University of Texas at Dallas, Richardson, TX 75080, USA
[4]LSPM-CNRS, Universite Paris Nord, 93430 Villetaneuse, France
[5]Ural Federal University, Mira str. 19, 620002 Ekaterinburg, Russia
[6]M.N. Mikheev Institute of Metal Physics UB RAS, S. Kovalevskaya str., 18, 620108 Ekaterinburg, Russia
[7]International Center for Materials Discovery, Northwestern Polytechnical University, Xi'an 710072, China
[8]CAS Key Laboratory of Functional Materials and Devices for Special Environments, Xinjiang Technical Institute of Physics & Chemistry, CAS, and Xinjiang Key Laboratory of Electronic Information Materials and Devices, 40-1 South Beijing Road, Urumqi 830011, China
[9]Center of Materials Science and Optoelectronics Engineering, University of Chinese Academy of Sciences, Beijing 100049, China
* S. Rahmanian Koshkaki and Z. Allahyari contributed equally to this work.
[§]Saeed.Koshkaki@skolkovotech.ru, [†]Z.Allahyari@skoltech.ru, [‡]A.Oganov@skoltech.ru

Abstract

Discovery of new magnetic materials is a big challenge to modern materials science. We report the development of a new extension of the evolutionary algorithm USPEX, enabling the search for half-metals (materials which are metallic only in one spin channel) and hard magnetic materials. First, we enabled the simultaneous optimization of stoichiometries, crystal structures, and magnetic structures of stable phases. Second, we develop a new fitness function for half-metallic materials which can be used for predicting half-metals through an evolutionary algorithm. Using this extended technique, we predict new potential hard magnets and rediscover existing half-metals. In total, we report five promising hard magnets with high energy product ($|BH|_{\mathrm{MAX}}$), anisotropy field (H_a), and magnetic hardness (κ) and a few half-metal phases of Cr-O system. Comparison of predictions with experimental results, including synthesis of a newly predicted antiferromagnetic material ($WMnB_2$), shows the robustness of our technique.

1 INTRODUCTION

Modern technology would be impossible without magnetic materials. Enhancing the useful properties of magnetic materials, while making them lighter and cheaper would facilitate applications of these materials in modern and future technologies. Two types of technologically appealing magnetic materials are considered here: hard magnets and half-metals. Discovery of hard magnets goes back 50 years, when permanent rare earth-based magnets were discovered [1]. Many technologies and devices were developed using these hard magnets, but in the past 30 years, there has been no significant achievement in the discovery of new hard magnets. At the same time, a new generation of electronic technology known as spin-electronics (spintronics) is emerging, with promise to utilize electron's spin degree of freedom to carry out logic operations and storage [2, 3]. 100% of spin-polarized current is the essence of this modern technology, so having new materials for producing fully polarized current at room temperature is a requirement.

One may divide ferromagnetic materials into two categories: *soft magnets* like annealed iron, which can be magnetized easily but also easily demagnetized, and *hard magnets*, which tend to stay magnetized. Permanent magnets are based on hard magnets such as alnico, ferrite (Fe_2O_3), or alloys of rare earth metals (i.e. Nd-Fe-B and Sm-Co types). There are four most important properties of a hard magnet: remanence (spontaneous magnetization M_0), Curie temperature T_c, coercivity (H_c), and energy product $|BH|_{MAX}$. These properties are determined by local magnetic moments, exchange interaction, and spin-orbit coupling. Hard magnets should include 1) heavy atoms to create strong spin-orbit coupling, a relativistic effect solely responsible for fixing the direction of magnetization— among thermodynamically stable elements, spin-orbit coupling is strongest in Bi, Pb, Re, W, Ta, Hf, rare earths, Sb, Sn, Cd, Ag, Mo, Zn — 2) transition metals — such as Fe, Co, Mn, or Ni — are good donors of spin density because of the nearly half-filled d orbitals, 3) some additional element to stabilize such a compound might be useful.

The scarcity of rare earth elements demands efforts to find high-performance magnetic materials without rare earth elements [4]. As such, searching for the promising magnetic structures and compounds of a material, using computational methods is advantageous since experiment is hindered by high cost and time-consuming procedure of synthesis, and it is in fact impossible to systematically search for promising materials only by experiment. By recent developments in computational/theoretical materials science[5, 6], several computational methods were proposed for automated screening based on density functional theory (DFT) coupled with either data mining procedures[7] or global optimization using, for example, evolutionary algorithms [8–12]. In this study, we extend our evolutionary algorithm USPEX[8, 9, 13, 14], and run magnetic structure prediction at spin-polarized generalized gradient approximation (GGA) [15] and GGA+U [16, 17] levels of theory. We performed variable-composition searches for stable ferromagnetic compounds containing a heavy atom to provide strong spin-orbit coupling, a transition metal to increase the number of unpaired electrons, and optionally an additional element to stabilize the compound. These calculations produced a set of stable compounds, with detailed chemical formulas, atomic and magnetic structures.

2 COMPUTATIONAL METHODS

The evolutionary algorithm (USPEX) used here, is capable of predicting stable structures/compositions formed by given atoms. Details of the method were described in Ref.[8, 9, 13], and a number of applications (e.g. [18–24]) illustrate its power for atomic and molecular crystals, surfaces, two-dimensional materials, polymers and nanoparticles. The variable-composition mode of USPEX [13] was used, allowing 16 maximum number of atoms per unit cell. 60% of the highest-ranked structures were allowed to produce offspring using different variation operators - heredity and mutation. In each generation (except the first generation), 40% of structures were generated using heredity, 40% were generated by mutation (15% by softmutation, 15% by transmutation, and 10% using spin mutation), and 20% were generated randomly. For binary systems (i.e. Cr-O, Fe-Sn, and Mn-Sn) the initial population size (number of ran-

domly generated structures in the first generation) is equal to 160 and the normal population size (number of structures of next generations) is equal to 80. For ternary systems (i.e. W-Mn-B), these numbers are increased to 200 and 120 respectively.

Underlying structure relaxations and energy calculations were done using the *Vienna Ab initio Simulation Package* (VASP) code [25–28] at zero-pressure. To reveal the ground state of magnetic materials, one needs to predict the optimal arrangement of local magnetic moments simultaneously with global optimization of the atomic structure, but an exhaustive sampling of all possible magnetic configurations for all produced crystal structures is often impractical. Here we simplified the problem by considering only collinear magnetic systems - ferromagnetic (FM), antiferromagnetic (AFM), ferrimagnetic (FiM), and non-magnetic (NM). Atoms in magnetically ordered phases can be in different spin states, high-spin (HS), low-spin (LS), various intermediate-spin states (IS), and in the same material different spin states can coexist (LH, LI, IH). To that end, a new operator, spin mutation, was added to vary the magnitude and direction of magnetic moments on randomly selected atoms (For details of this new operator please refer to the supplemental material).

Many magnetic materials are strongly correlated and one often has to go beyond DFT or DFT+U approaches. For several found materials, we carefully took electronic correlations into account using the DFT+U method [29–32] and the the dynamical mean-field theory (DMFT) [33, 34]. This approach provides a systematic treatment of many-body effects by considering the local spin dynamics. A combination of DFT and DMFT, known as DFT+DMFT approach [35], has become a state-of-the-art method for realistic description of correlated materials (for a review, see [36, 37]). Our DMFT calculations were performed in the paramagnetic (spin symmetric) phase using the AMULET code [38]. The impurity problem was solved by the hybridization-expansion continuous-time quantum Monte Carlo algorithm with the density-density form of Coulomb interaction. The double-counting correction was taken in the around mean-field form. The Coulomb interaction matrix for d-shells was parameterized via Slater integrals F^0, F^2, F^4 linked to the Hubbard $U = F^0$ and Hund's rule coupling $J = (F^2 + F^4)/14$ (details

can be found in [39]).

In order to study half-metals, accurate band gaps are needed, and for this reason, the HSE06[40, 41] hybrid functional was used to calculate band structures and density of states of the discussed Cr-O phases (see Fig. S4), using the PWmat[42, 43] code. The spin-polarized calculations were done using NCPP-SG15-PBE pseudopotential with energy cutoff of 680 eV and appropriate Monkhorst-Pack k-mesh with the resolution of $2\pi\times$ 0.06 Å^{-1}.

2.1 Hard magnets

For all selected systems, after finding the best structures using USPEX with $U - J$ = 0 eV, the top 60-80 ranked structures were chosen for further investigation of their hard magnetic properties. To explore electron correlation effects, all selected structures were relaxed again at different values of $(U - J)$. An important measure we used to find hard magnetic properties is the magnetocrystalline anisotropy energy (MAE) curve. The MAE curve was calculated using a computationally efficient method implemented in VASP. In this method, initially, we do a high-precision magnetic calculation (collinear calculation) to obtain magnetic ground state, charge density, and wavefunction, then we added spin-orbit coupling and used the charge density and wavefunction obtained in the first step for calculating ground state energy for different magnetization direction (non-collinear calculation). In this method, to optimize the calculation time, the initial calculation (collinear) is performed self-consistently, and then for the rotation of the magnetization direction (non-collinear), the non-selfconsistent method implemented in VASP was used [44]. (For more detail on convergence of MAE curve calculation please refer to the supplemental materials).

For DFT+U calculations, we used Dudarev's formula [17], which needs only one parameter, i.e. $(U - J)$, in running the DFT+U calculation. In finding the MAE curve, we used the plane wave kinetic energy cut-off of 600 eV and for each material and different values of $U - J$ we carefully checked the energy convergence with changing k-point meshes density to get excellent convergence of the energies

and structural parameters. All the studied compounds are metallic and one expects that on-site electron correlations of $3d$-electrons are to a large extent (but not completely) screened. We explored these phases at $0 \leq$U-J$\leq 2\ eV$ to account for the uncertainty of the extent of electron correlation in each compound. We then calculated the MAE curve, maximum energy product $|BH|_{\mathrm{MAX}}$, magnetic hardness, and the anisotropy field (H_a) for selected structures. In the calculation of the MAE curve and anisotropy constants, we used an automatic k-point generator implemented in VASP and rotated the magnetization angle to find directions with the lowest and highest energy. The difference between these two energies gives MAE and the curve connoting them is called the MAE curve. To calculate the MAE curve and subsequently hard-magnetic properties, we used the uni-axial anisotropy expression; this approximation provides a simple but powerful parameterization of the magnetic anisotropy [45]. In this approximation, MAE curve can be quantified by fitting energies to the following expression:

$$\frac{E}{V} = K_1 \sin^2 \alpha + K_2 \sin^4 \alpha, \tag{1}$$

where K_1 and K_2 are the first and second anisotropy constants, α is the angular change along the MAE curve and V is the volume of the unit cell. Using this approximation two different types of anisotropy are possible, namely easy axial and easy planar anisotropy. In easy axial anisotropy $K_1 < 0$ and for easy planar anisotropy $K_1 > 0$, thus here we report absolute values of K_1 and K_2 but we mention easy axial/planar in a separate column of table 2

For each magnetic structure, we can define the magnetization vector in the Cartesian coordinate system as:

$$M = M_0(\sin\theta\cos\phi\hat{x} + \sin\theta\sin\phi\hat{y} + \cos\theta\hat{z}), \tag{2}$$

where M_0 is spontaneous magnetization and $(\hat{x}, \hat{y}, \hat{z})$ are coordinates of the unit vector of magnetization, θ and ϕ are the angles of Cartesian coordinates retrieved from spherical coordinates (radius M_0, inclination θ, azimuth ϕ). Using the single-domain crystal assumption with coherent rotation of magnetization for ferromagnetic phases, we compute the anisotropy field in the ferromagnetic Stoner-Wohlfarth model

(SW):

$$H_a = 2\frac{K_1}{\mu_0 M_0}, (K_1 > 0) \tag{3}$$

Here, we ignored K_2 since all predicted materials in this work have $K_2 \approx 0$. By calculating magnetization M_0, one can calculate the energy product ($|BH|_{\mathrm{MAX}}$) which is the absolute upper limit of magnetostatic energy stored in free space by a permanent magnet of unit volume [45]. $|BH|_{\mathrm{MAX}}$ for an ideal square hysteresis loop [4] is given by,

$$|BH|_{\mathrm{MAX}} = \frac{\mu_0 M_0^2}{4}, \tag{4}$$

where μ_0 is permeability ($\mu_0 = 4\pi \times 10^{-7} NA^{-2}$).

Another important quantity in characterizing hard magnets is the possibility to fabricate a magnet in any shape without losing its magnetization [4], this dimensionless quantity is known as magnetic hardness (κ),

$$\kappa = \sqrt{\frac{K_1}{\mu_0 M_0^2}} \tag{5}$$

for an optimized single-domain permanent magnet to have $H_c > M_0/2$, a value of $\kappa > 1$ is expected (this condition may change depending on the desired macroscopic shape of the magnet, e.g. long needle, thin-film, etc).

2.2 Half-metals

In order to get high signal strength and robust readout in spin-electronic devices, having fully polarized current is an ideal [46, 47]. One way to get 100% polarization is to use half-metals as spin filter. Half-metals have the intrinsic ability to produce spin-polarized electronic current. In a half-metal, the density of states (DOS) at Fermi level $g(E_f)$ for one spin direction is zero (usually minority band) and the other spin direction has non-zero $g(E_f)$ (one spin channel is insulating while the other is conducting) [48]. In 1983 de Groot et al reported half-metallic Heusler alloys as a new type of magnetic materials [49]. Since then, many other discoveries, both theoretical and experimental, of half-metals were reported, including

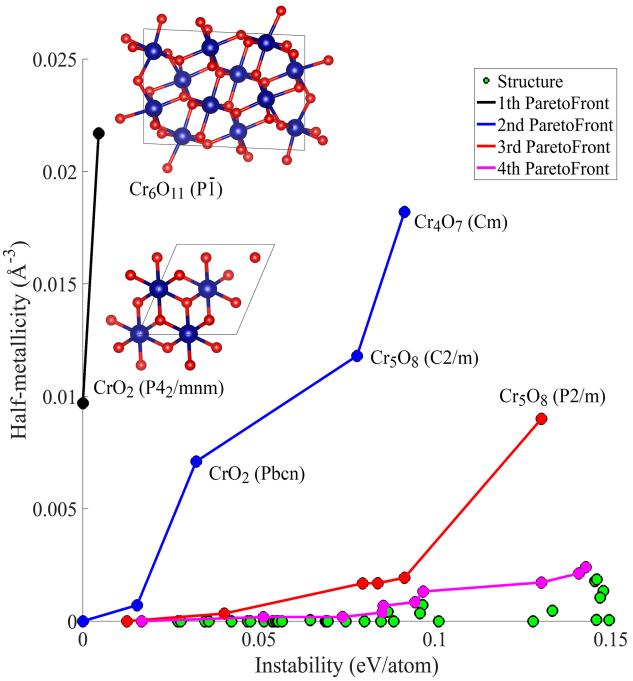

Figure 1: Ashby plot of half-metallicity vs. instability of Cr-O structures. Structures on the first Pareto front are shown.

two famous half-metals: rutile-structured CrO_2 and Heusler alloy NiMnSb [48]. While many works have tried to predict new half-metals candidate [50–54], still, a reliable, fast, low-cost and general method of discovery is lacking. One of the main disadvantages of current half-metals is the high temperature dependence of current polarization, which has roots in spin wave excitation and a narrow gap between Fermi energy and top of the conduction band in the insulating channel [47].

Using the density of states (DOS) at Fermi energy, we define the spin polarization to be [55]:

$$P(E_f) = \left| \frac{\rho_\uparrow(E_f) - \rho_\downarrow(E_f)}{\rho_\uparrow(E_f) + \rho_\downarrow(E_f)} \right| \tag{6}$$

where $\rho_\uparrow(E_f)$ and $\rho_\downarrow(E_f)$ are density of states at Fermi level for either of spin channels. One major reason for this temperature dependence is the location of the Fermi energy near the top (bottom) of valence (conduction) band in the insulating channel. In this section, we introduce our new fitness function to remove this barrier. To have 100% spin polarization, one spin channel should be insulating (semiconducting) and the other one conducting. Also to have good conductivity, the conducting spin channel

should have high enough DOS at Fermi level ($\rho(E_f)_{\rm cond}$). The fitness that embodies all this information in the form of a single number is (with unit of Å^{-3}),

$$f_{HM} = (\frac{E_C \times E_V}{E_g})_{\rm ins} \times (\rho(E_f))_{\rm cond} \tag{7}$$

where E_C and E_V is the energy difference between Fermi energy and bottom of conduction band and top of the balance band respectively, E_g is the energy bandgap ($E_g = E_C + E_V$), $(\rho(E_f))_{\rm cond}$ is the density of states (in states/eV·Å^3) for conducting spin channel (all E_g, E_C and E_V are defined for insulating channel). The advantage of this new fitness is that it can measure band gap and DOS simultaneously.

Multi-objective (MO) optimization [56, 57] mode of USPEX was used to ensure that structures obtained through the evolutionary search are both good half-metals and energetically favorable. It is important to use this method since unstable half-metal compounds are as useless as stable compounds with no half-metallicity, and both properties need to be optimized simultaneously − see Fig. 1.

3 RESULTS

3.1 Half-metals

To test our fitness and new extension to USPEX, we chose the well-studied Cr-O system. In this system we expect to find the known half-metal CrO_2. In this calculation, we employed multi-objective optimization method [56, 57] in order to search for phases with low energy and high half-metallicity simultaneously. We performed USPEX search in the Cr-O system using GGA-PE functional [15] with $U - J$ = 2.1 eV and 3.7 eV (typical values used by previous studies on this system [58–60]). These calculations were done using the variable-composition mode [13] of USPEX, to screen all the possible compounds in this system. As a result, several promising phases were predicted. Among these, all the reported stable phases [61] were indeed found. Our calculations show that $R\bar{3}c$-Cr_2O_3 is stable at both $U - J$ = 2.1 and 3.7 eV, which is in agreement with previous studies [58, 59]. $P4_2/mnm$-CrO_2 is stable at $U - J$ = 2.1 eV and metastable (45 meV/atom above convex hull) at $U - J$ = 3.7 eV. Several geometrically similar CrO structures with space groups $Cccm$, $C2/c$ and $P4_2/mmc$ were predicted. Our calculation shows

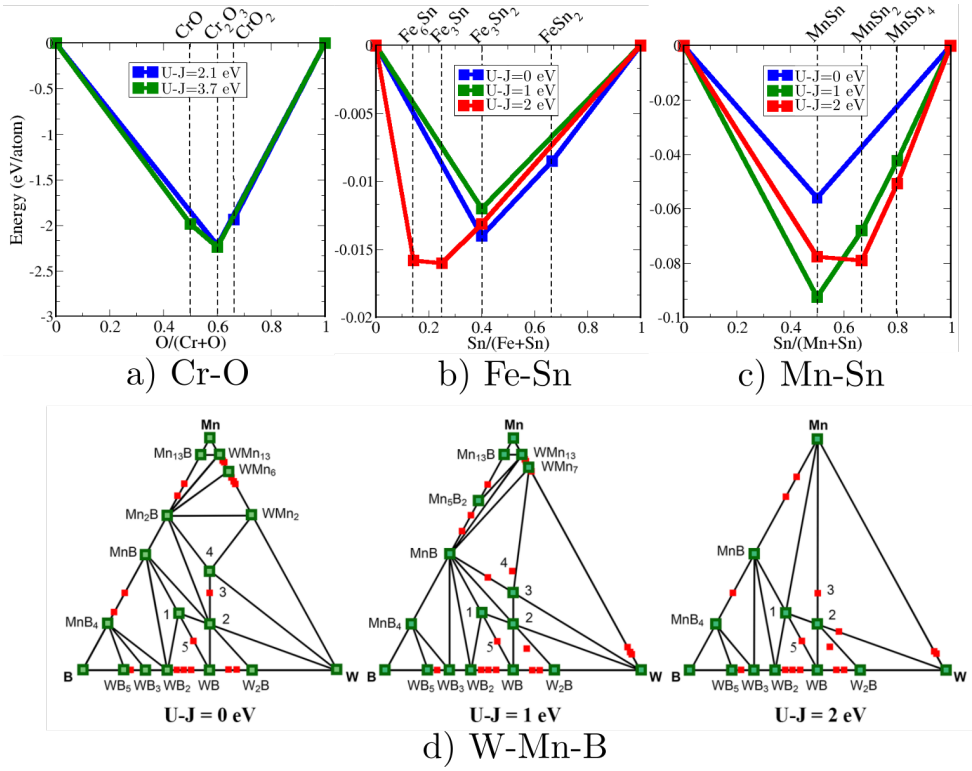

Figure 2: Convex hulls of (a) Cr-O, (b) Fe-Sn, (c) Mn-Sn and (d) W-Mn-B systems.In ternary case, green points indicate stable phases, red points show metastable phases. It is worth mentioning that the stability of one structure with one value of $U - J$ does not guarantee stability for other values of $U - J$, for more detail of the range of stability of selected compound with the change of $U - J$, check the supplemental material.

that the energy of $Cccm$-CrO is slightly lower, and this structure is thermodynamically stable at $U - J$ = 3.7 eV and metastable at $U - J$ = 2.1 eV (12 meV/atom above convex hull). The phase diagram of this system is shown in Fig. 2a. We find that Cr_5O_{12} is metastable with the energy 17 meV/atom and 133 meV/atom above convex hull for $U - J$ = 2.1 and 3.7 eV, respectively (In agreement with other work arguments [62]). In addition to prediction of all reported low-energy chromium oxides, we predicted several new promising phases with low energy and/or high half-metallicity. Metastable low-energy phases $P\bar{1}$-Cr_3O_4 (with energy 15 meV/atom above the convex hull), and $C2/m$-Cr_5O_8, $P2/m$-Cr_5O_8 and Cm-Cr_4O_7 with high half-metallicity were predicted by our calculations and are shown in Table 1.

Looking at Table 1, one can see that several phases are predicted with high half-metallicity. The predicted $P4_2/mnm$-CrO_2 found to be a half-metal, and its crystal structure is in excellent agreement with experiment [63, 64] (see Table 1). Along with this phase, two very promising half-metal phases are Cr_6O_{11} and Cr_4O_7 with energies very close to the convex hull. All these phases are also predicted to have high magnetization. In recent years, many attempts on discovery of new half-metal − from 2D systems [52, 53] to Heusler alloys[51] − have been made. In this work, we defined a simple and physically reasonable fitness for half-metals and showed that the extension of evolutionary algorithm USPEX by the introduced fitness, makes a powerful tool for systematic search for this class of materials and can facilitate discovery of new half-metals.

3.2 Hard magnets

Below we present results of the search for stable hard magnets. One has to keep in mind that finding rare earth-free hard magnets is a challenging task, here we picked stable and metastable phases, which have at least one of the selected hard magnets properties, i.e. spontaneous magnetization (M_0), anisotropy field (H_a), magnetic hardness (κ) and energy product ($|BH|_{\mathrm{MAX}}$). As a benchmark we also calculate the hard magnetic properties of FePt, a well-known hard magnet, and our results are in very good agreement with actual properties of FePt, see Table. 2.

Compounds	**space group**	**Magnetization** $\mu_B \cdot^{-3}$	$f_{HM} \times 10^3$ $^{-3}$	**Lattice parameters** a(Å)	b (Å)	c (Å)	α	β	γ	**ΔH** (eV/atom)	**E above convex hull** (eV/atom)
CrO_2	$P4_2/mnm$	0.068	9.7	4.49	4.49	2.98	90.0	90.0	90.0	-1.935	0
Cr_2O_3	$R\bar{3}c$	0.115	0.0	5.09	5.09	13.76	90.0	90.0	120.0	-2.216	0
Cr_6O_{11}	$P\bar{1}$	0.081	21.7	9.58	7.06	5.45	72.3	81.1	89.7	-2.013	0.004
CrO	Cccm	0.147	0.0	4.02	4.69	5.46	90.0	90.0	90.0	-1.834	0.012
Cr_3O_4	$P\bar{1}$	0.120	0.7	5.43	3.05	5.16	88.3	73.3	96.0	-2.095	0.015
CrO_2	Pbcn	0.069	7.1	4.31	5.51	5.02	90.0	90.0	90.0	-1.903	0.032
Cr_2O_3	$R\bar{3}$	0.108	0.0	5.15	5.15	14.37	90.0	90.0	120.0	-2.162	0.055
Cr_5O_8	C2/m	0.095	11.8	10.10	2.96	10.16	90.0	105.2	90.0	-2.073	0.078
Cr_4O_7	Cm	0.069	18.2	12.32	3.03	10.08	90.0	129.5	90.0	-1.971	0.091
Cr_5O_8	P2/m	0.091	9.0	5.21	3.00	9.90	90.0	100.3	90.0	-2.021	0.130
Experimental											
CrO_2[65]	$P4_2/mnm$			4.42	4.42	2.92	90.0	90.0	90.0	-2.066[66]	0
Cr_2O_3[67]	$R\bar{3}c$			4.96	4.96	13.60	90.0	90.0	90.0	-2.340[68]	0

Table 1: Properties of the predicted chromium oxides at $U - J$ = 2.1 eV.

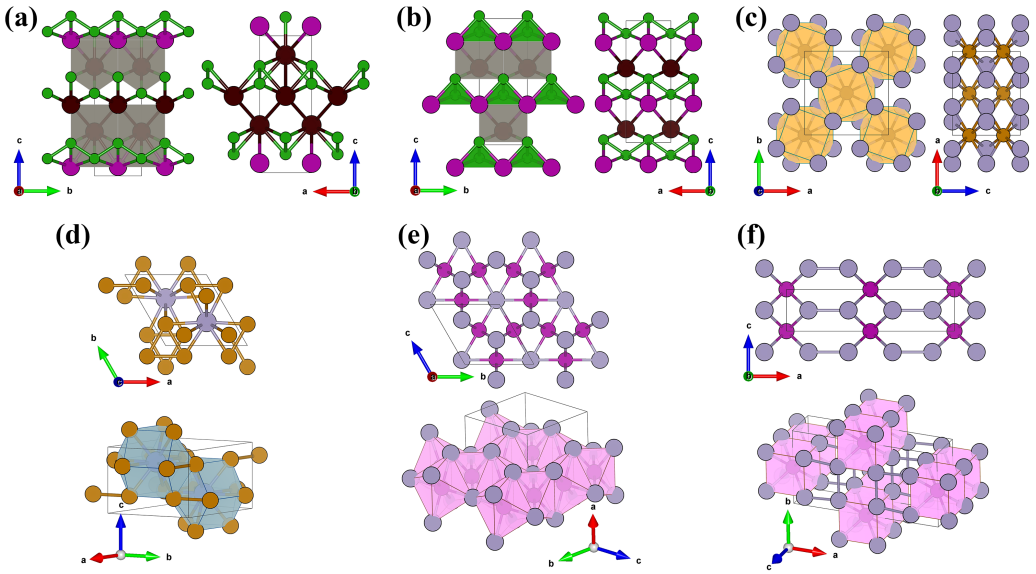

Figure 3: Crystal structures of studied magnetic systems: (a) *Pmm2*−W_3MnB_4, (b) *Amm2*−$WMnB_2$, (c) *I4/mcm*−$FeSn_2$, (d) *P6$_3$/mmc*−Fe_3Sn, (e) *P6/mmm*−MnSn, (f) *Cmmm*−$MnSn_4$. Black atoms are W, purples are Mn, grays are Sn, golds are Fe, and greens are B. For better insight, each crystal structure is shown from two views.

3.2.1 W-Mn-B SYSTEM

In W-Mn-B systems, tungsten plays the role of a heavy element, and manganese is a donor of spin density. Boron was added to search a broader space and stabilize additional compounds. We used the evolutionary algorithm USPEX with $U - J = 0$ eV to search for stable compounds in the W-Mn-B in 80 generations (exploring about 9600 structures with different stoichiometry). All the energy calculations and structure relaxations in USPEX were done using VASP spin-polarized method with the GGA-PBE functional.

In this system, several stable/metastable compounds were predicted. In the energy calculation for different $U - J$, we found several promising compounds in non-zero ranges of $U - J$ and plotted the ternary convex hull diagram as shown in Fig. 2d. Among the predicted ternary compounds, we found two promising antiferromagnetic and ferromagnetic phases: $WMnB_2$, and W_3MnB_4, respectively. Of these, $WMnB_2$ turned out to be stable at different values of $U - J$ and W_3MnB_4 found to be metastable

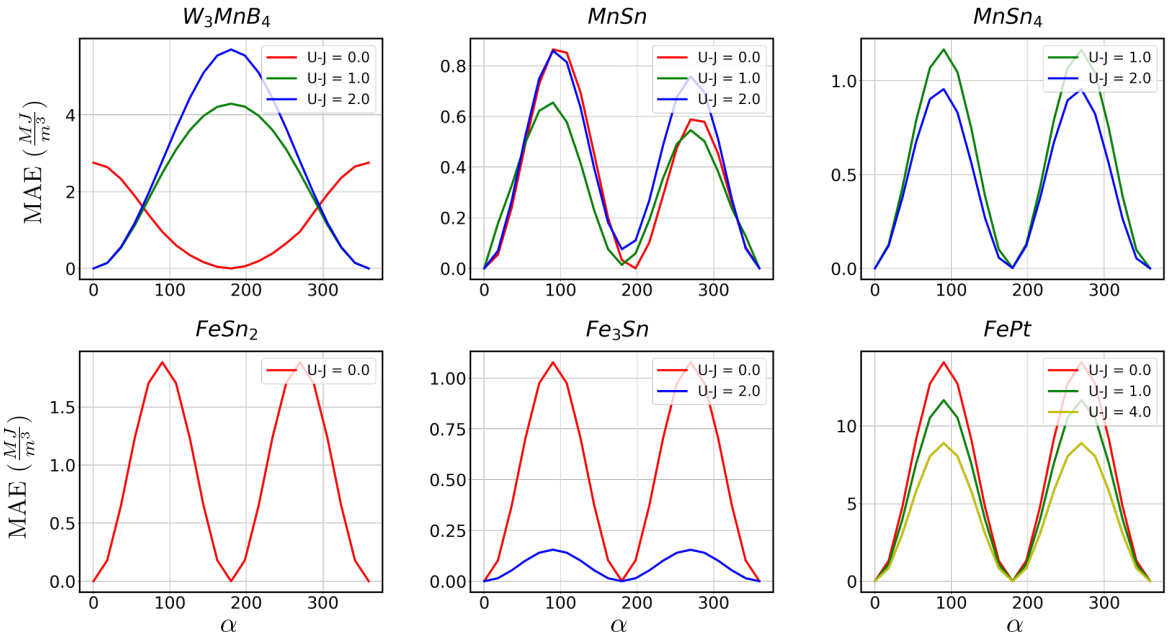

Figure 4: MAE curves for each stable phase and different $U - J$ values.

with very low energy — for example, 7 meV/atom above the convex hull at $U - J$ =0 eV. Another predicted phase, W_2MnB_2, is not a promising hard magnet, but it is experimentally synthesized [69, 70] and our calculations have successfully predicted this compound to be stable at all values of $U - J$. The experimental P_4/mbm structure [69] is found to be stable at $U - J \geq 0.3$ eV (Table 2), whereas a new $Immm$ polymorph is stable at $(U - J) < 0.3$ eV. Crystal structures of all ternary compounds, studied in this work, are shown in Fig. 3.

W_3MnB_4 The predicted W_3MnB_4 has the $Pmm2$ space group (Fig. 3a), and theoretically shows a very large MAE and H_a that is created by spin-orbit coupling. Although W_3MnB_4 for all values of $U - J$ has a very large MAE (comparable to rare-earth permanent magnets), this compound in pure form is not a good candidate for permanent magnets since it doesn't have uni-axial anisotropy. But using techniques such as megajoule magnets [71, 72] (where hard and soft magnets are coupled in a nanostructure composite) or optimization of structure with a fourth element a uni-axial anisotropy and larger energy product can be achieved. We report the hard-magnetic properties for this material in table

2 assuming MAE= K_1.

$WMnB_2$ Second ternary compound, which shows stability for all values of $(U - J)$, is $WMnB_2$. This compound was first predicted with $U - J$ = 4 eV, at which the stable phase has space group $P2_1/m$. Running calculations with $(U - J)$ below 3 eV, we found other stable structure. For $U - J$ = 0 eV the stable structure has space group $I\bar{4}m2$, for $U - J$ = 1 eV space group $Pmmn$ and for $U - J$ = 2 eV, space group $Amm2$ (Fig. 3b). Experimental synthesis yielded the latter structure, but found no magnetization.

In structure prediction calculations with up to 16 atoms in the primitive cell, $WMnB_2$ was found to be stable in the ferromagnetic state. Our DFT+U calculation, however, does not exclude antiferromagnetic solutions with larger cells [73]. Indeed, susceptibility calculations (Fig. 5(a)) indicated the preference of antiferromagnetic order (supported by explicit calculations of antiferromagnetic ordering and by experiment, see below). If $WMnB_2$ were ferromagnetic (and perhaps, a ferromagnetic state can be induced by doping or strain), it would be a hard magnet.

DMFT for $WMnB_2$ To explore magnetic properties of $WMnB_2$ and to shed light on some of its electronic properties (see Supplementary Information), we consider the electron correlations using the DFT+DMFT approach. For Mn $3d$ states we adopt $U = 3$ eV and $J = 0.9$ eV used in previous DMFT studies of γ-Mn [74, 75], while smaller values $U = 2.5$ eV and $J = 0.5$ eV were taken for tungsten due to stronger screening in the $5d$-elements. Our DMFT calculations explicitly include the $3d$, $4s$, and $4p$ states of Mn, $5d$ and $6s$ states of W, $2s$ and $2p$ states of B, by constructing a basis set of site-centered Wannier functions as described in Ref. [76].

Using the DFT-Hamiltonian matrix H_{DFT} in the basis of Wannier functions and the self-energy Σ, obtained in DMFT approach, we calculate the momentum dependence of the magnetic susceptibility in the zeroth order in the interaction vertices (particle-hole bubble)

$$\chi^0_{\mathbf{q}} = -(2\mu_B^2/\beta) \sum_{\mathbf{k},\nu_n,ij,mm'} G^{im,jm'}_{\mathbf{k}}(i\nu_n) G^{jm',im}_{\mathbf{k+q}}(i\nu_n), \tag{8}$$

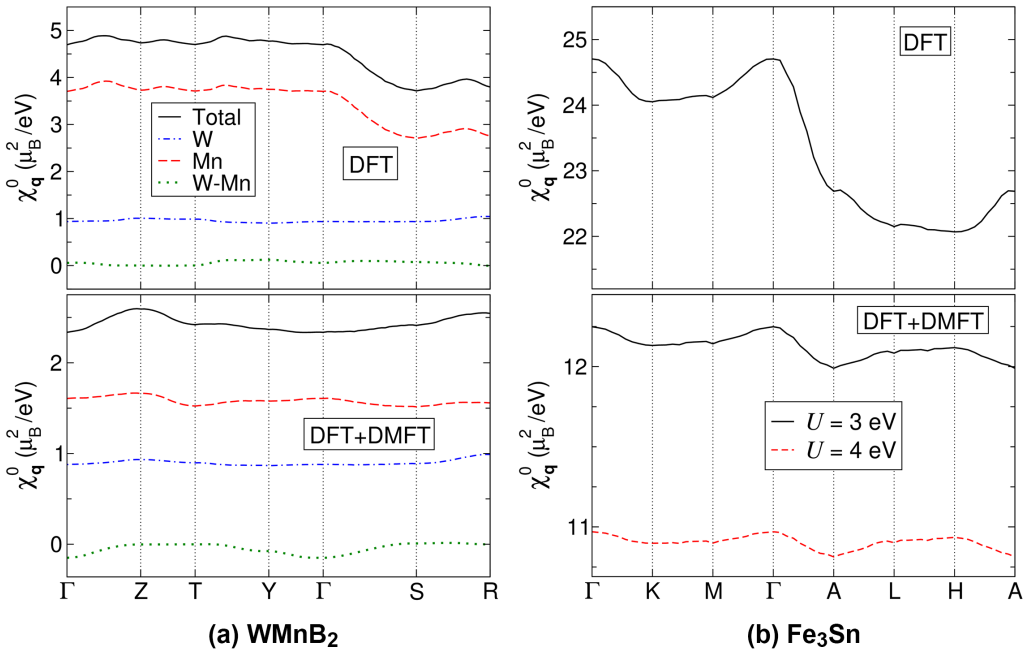

Figure 5: Momentum-dependent susceptibility of (a) $WMnB_2$, and (b) Fe_3Sn obtained by DFT and DFT+DMFT at $\beta = 20$ eV^{-1} for $WMnB_2$, and $\beta = 10$ eV^{-1} with different values of Hubbard U and fixed $J = 0.9$ eV, for Fe_3Sn.

where $\beta = 1/T$ is the inverse temperature, $G_{\mathbf{k}}(i\nu_n)^{im,jm'} = [(\mu + i\nu_n)I - H_{\rm DFT}(\mathbf{k}) - \Sigma(i\nu_n)]^{-1}_{im,jm'}$ is the one-particle Green's function for wave vector $\mathbf{k}$ and fermionic Matsubara frequency $\nu_n = (2n+1)\pi/\beta$, μ is the chemical potential, I is the unit matrix, i and j are site indexes, m and m' are orbital indexes. We have verified the convergence of the obtained results with respect to the density of the grid in momentum space. The obtained $\chi^0_{\mathbf{q}}$ is shown in Fig. 5a. One can see that in DFT ($\Sigma = 0$) the maximum of the particle-hole bubble is achieved at the incommensurate wave vectors in $\Gamma-$Z and T$-$Y directions. Near these maxima the bubble is characterized by rather weak momentum dependence, such that close competition between ferromagnetic and these incommensurate correlations is expected. At the same time, in DMFT we find stronger momentum dependence of the particle-hole bubble, with the maxima, located at wave vectors, corresponding to Z and R points of the Brillouin zone. Therefore, according to these DMFT results the antiferromagnetic order with the above mentioned wave vectors is expected to be dominant.

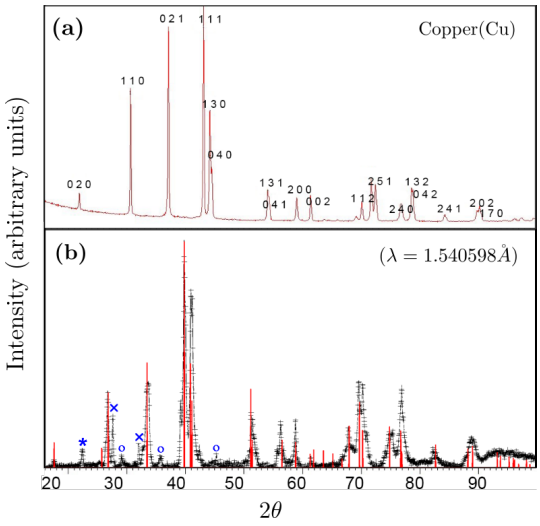

Figure 6: (a)X-ray diffraction pattern showing 100% yield of $WMnB_2$, (b) X-ray diffraction pattern of $WMnB_2$ synthesized at 5.2 GPa and 2500 K. Vertical red ticks correspond to expected positions and intensities of diffraction lines of the orthorhombic $Amm2$ structure predicted with $U - J$ = 2 eV. Blue asterisk, crosses and circles correspond to graphite, WC ($P\bar{6}m2$) and WB ($I4_1/amd$) impurities, respectively.

Synthesis of $WMnB_2$ Very few studies focused on the W-Mn-B system, mostly in 1960-1970s[69, 70, 77]. The latest of these works[70] concludes that the following ternary compounds are stable: $(W,Mn)_3B_2$ (U_3Si_2-type structure), W_4MnB_5 (CrB-type structure with homogeneity region 38-42 at.% W, 8-12 at.% Mn), and WMnB with unknown structure. Our calculations, however, predict that $WMnB_2$ should be stable as well, and we decided to test this prediction experimentally.

In order to determine precisely the structure of $WMnB_2$, the structure of recovered pellet samples from High-pressure experiments (see the Supplementary Information), was studied by powder X-ray diffraction using Equinox 1000 Inel diffractometer (Bragg-Brentano geometry, Cu Kα radiation). Lattice parameters have been derived from the Le Bail profile refinement procedure [78] performed using the PowderCell software. Characteristic diffraction pattern of the single-phase $WMnB_2$ sample is shown in (Fig. 6b). The lattice parameters are $a = 3.012(2)$ Å, $b = 3.120(1)$ Å and $c = 8.130(8)$ Å (in the $Amm2$ setting), or $a = 3.120(1)$ Å, $b = 8.130(8)$ Å, and $c = 3.012(2)$ Å (in the $Cmcm$ setting), in excellent agreement with the above described experiment and with theoretical prediction. The only

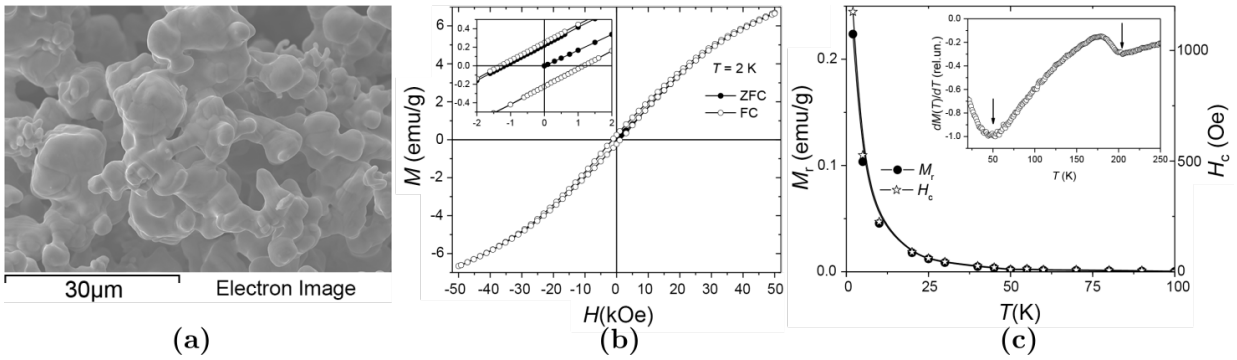

(a) (b) (c)

Figure 7: (a) sample under electron microscope (x3000), (c) Isotherms M(H) of $WMnB_2$ at $T = 2K$. Sample was cooled from $T = 300K$ down to $2K$, at which the magnetzation curve was measeured (ZFC - cooling was done at $H \approx -8Oe$, FC - at $H = 50kOe$) (d) Temperature dependence of the remanence M_r and coercivity H_c of $WMnB_2$. Inset: temperature dependence of the derivative $dM(T)/dT$. The arrows correspond to the expected magnetic phase transition temperatures.

difference is that our predicted structure is fully ordered, whereas in experiment (due to high temperatures of synthesis) the same crystal structure was obtained, but with W-Mn disorder (hence higher symmetry $-Cmcm$ vs $Amm2$).

Measurements of magnetization indicates that $WMnB_2$ is not a ferromagnet in its ground state. The shape of the hysteresis loop (Fig. 7b) is not typical of an antiferromagnet either, and we think that this material has both ferro and antiferromagnetic interactions and is closer to the antiferromagnetic state. At 2 K in fields $H >$30-40 kOe, there is a difference between the ZFC curve and the field-down branch of the hysteresis loop, which indicates a strong magnetic anisotropy in the antiferromagnetic state. Non-linearity of M(H) is strongest at low temperatures, while the magnetization curves are close to linear at temperatures above 100 K. Both the coercivity H_c and remanence M_r decrease fast with increasing temperature (Fig. 7c). Temperature dependence of the derivative $dM(T)/dT$ shows two possible phase transitions, one at 50 K and the other at 200 K (Inset in Fig. 7c). At 50 K we observe disappearance of the hysteresis, but, according to the magnetic susceptibility data, ferro and antiferromagnetic interactions persist at higher temperatures. The anomaly at 200 K is likely due to to the Neel transition from the antiferromagnetic to the paramagnetic state (which, however, still has small parasitic ferromagnetism).

3.2.2 Fe-Sn SYSTEM

Alongside ternary systems, we also explored two binary systems, Fe-Sn and Mn-Sn, where tin is a heavy metal needed for strong spin-orbit coupling and iron or manganese are donors of the spin density. We searched for low-energy structures of these systems using the evolutionary algorithm USPEX for 60 generations (by exploring around 5000 structures with different stoichiometries). Details of ab initio calculations are similar to W-Mn-B calculations and are explained in the previous section. In these calculations, several promising stable and low-energy metastable structures were found at different $U-J$ — see the convex hull diagram of the Fe-Sn system in Fig. 2b.

For $U-J$ = 0 eV, it turned out that two compounds: $FeSn_2$ and Fe_3Sn_2 are stable, while there are no other metastable compounds close to the convex hull. Fe_3Sn_2 was found to be stable at all values of $U-J$, and its crystal structure is known experimentally to be $R\bar{3}m$ [79], which is in agreement with our prediction for $(U-J) < 1.8$ eV. Our calculations predict Fe_3Sn_2 to be a ferromagnet (in agreement with experiment [80, 81]), but the calculated MAE for all $U-J$ is at least an order of magnitude larger than experimental [80, 81]. At $U-J$ = 1 eV, several metastable compounds were predicted, while none of them showed the properties of a hard magnet.

Similarly, several metastable compounds, such as Fe_7Sn, Fe_6Sn, Fe_8Sn, Fe_5Sn, and Fe_4Sn, were found at $U-J$ = 2 eV. Our calculations show that at $U-J$ =2 eV, Fe_3Sn is promising for being hard magnets. Of metastable compounds, Fe_4Sn turned out to be antiferromagnetic and Fe_8Sn, Fe_7Sn, Fe_5Sn, and Fe_6Sn have a very low anisotropy constant. (For more details on structures of these compounds, see the Supplementary Material).

$FeSn_2$ For $FeSn_2$ with $U-J$ = 0 eV, we found metastable phases with space groups $I4/m$, $P1$, $C2/c$, $C2/m$ and a stable phase with space group $I4/mcm$. The stable phase also shows interesting hard magnet properties, and its crystal structure is in excellent agreement with the experimental data (Table 2). Our prediction of the MAE for this phase is 1.88 MJ/m^3 with easy plane anisotropy, which is not

desirable for permanent magnets; its crystal structure is shown in Fig. 3c. This phase can be studied more about whether an easy-axis anisotropy is achievable or not and how to improve energy product by adding a third element to increase magnetization. Other properties of this phase are listed in Table 2.

Fe_3Sn This compound has two competitive structures, both with space group $P6_3/mmc$, one with 2 and the other with 4 formula units in the unit cell. Here we study the former structure as it has higher magnetization and is stable at $U - J$ = 2 eV (Fig. 3d). This phase is stabilized by on-site electron correlation and it is stable only at $U - J > 1.7$ eV. For this phase, structural properties are again in good agreement with experimental results (Table 2). Previous DFT calculations and experimental result [81] showed that this compound has a large MAE of 1.59 MJ/m^3, but here we performed the DFT+U calculation of MAE with $U - J = 0, 2$. Interestingly the MAE we calculated for $U - J$ = 0 ($\approx 1.1 MJ/m^3$) is in the same order of the result in [81] but our calculations shows that Fe_3Sn is a thermodynamically metastable phase at $U - J$ = 0 (it is 0.035 eV/atom above the convex hull), on the other hand, for the stable phase with $U - J$ = 2 our calculations shows that Fe_3Sn has negligible MAE ($\approx 0.16 MJ/m^3$) but large $|BH|_{\mathrm{MAX}}$, up to 545 $KJ.m^{-3}$ for the stable phase with an easy axis anisotropy. This means for $P6_3/mmc$–Fe_3Sn, increasing $U - J$ would stabilizes the structure but worsen the hard magnetic properties.

For further insight into the magnetic properties of Fe_3Sn, we take into account the electron correlations using the DFT+DMFT approach. We use $U = 3$ eV and $J = 0.9$ eV, which are in agreement with estimates for elemental iron [82]. We also consider larger $U = 4$ eV to make sure that our choice of the $U - J$ parameter does not qualitatively affect the results. In our DMFT calculations we explicitly include the $3d$, $4s$, and $4p$ states of Fe and $5s$, $5p$ states of Sn, by constructing a basis set of site-centered Wannier functions as described in Ref. [76].

In Fig. 5b we present the momentum dependence of the particle-hole bubble $\chi^0_{\mathbf{q}}$ calculated by Eq. (8). In DFT we find clear peaks of the particle-hole bubble at $\mathbf{q} = 0$, which show that the ferromagnetism

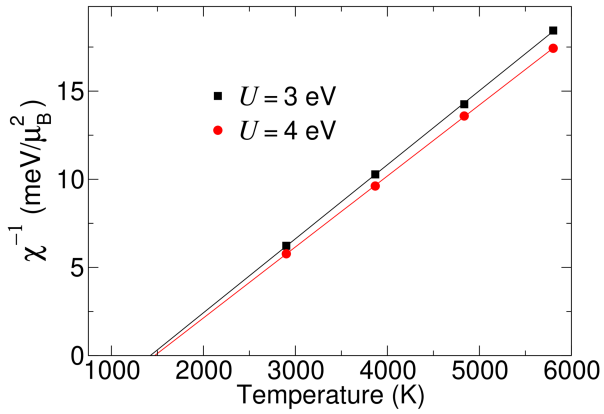

Figure 8: Inverse uniform magnetic susceptibility of Fe_3Sn as a function of temperature obtained by DFT+DMFT with different values of Hubbard U and fixed $J = 0.9$ eV.

is expected to be the dominant instability for this compound. The peaks of the particle-hole bubble at the Γ point are also preserved in DFT+DMFT analysis, which yields, however, closer competition of the obtained ferromagnetic order with spin-density-wave correlations, characterized by the wave vector $\mathbf{q}_{\mathrm{H}}$.

Next we calculate the uniform magnetic susceptibility as a response to a small external field introduced in the DMFT part. We find (see Fig. 8) linear temperature dependence of inverse susceptibility with the theoretical Curie temperature $T_{\mathrm{C}} \approx 1500$ K, which weakly depends on Hubbard U. At present, most material-specific DMFT calculations consider the Coulomb interaction in the density-density form, which corresponds to the Ising symmetry of Hund's exchange. This approximation drastically reduces the computational costs making such calculations feasible. However, it leads to an overestimation of the Curie temperature [83]. Moreover, the mean-field nature of DMFT also contributes to the overestimation of Curie temperature, that can only be overcome by sophisticated approaches beyond DMFT. Previous DFT+DMFT studies of metallic iron found that two above-mentioned approximations lead to about twofold overestimation of its Curie temperature [82, 84]. Assuming the same ratio of calculated and experimental Curie temperatures, we obtain a rough estimate of the Curie temperature for Fe_3Sn to be $\sim$750 K, which is very close to the experimentally measured $T_c = 725$ K [81].

3.2.3 Mn-Sn SYSTEM

The Mn-Sn system thermodynamic convex hulls for all ($U - J$) values are shown in Fig. 2c. In this system there are multiple stable and metastable phases, some of which we show to be a good candidate for permanent magnets production. Among the predicted phases, $MnSn_2$ (a experimentaly synthesized phase in Mn-Sn system) is stable at 0.6 $eV \leq U - J$ and its crystal structure is correctly predicted in our calculations (Table 2), however, this compound is not a promising hard magnet. Below we report on two promising hard magnet candidates with easy-axis anisotropy for some of $U - J$'s.

MnSn This phase has space group $P6/mmm$ (Fig. 3f) and is stable at all values of ($U - J$) explored here. For $U - J$ = 0 eV, this phase has an easy axis anisotropy but for $U - J$ = 1, 2 eV, it has easy plane anisotropy. MnSn has a decent value of anisotropy field and MAE compared to rare earth hard magnets and suggests this phase can be a good candidate for a cheap hard magnet. MnSn shows the largest spontaneous magnetization among all compounds studied in this work (comparable to Sm-Co hard magnets). For other magnetic properties of this phase, see Table 2.

$MnSn_4$ This compound showed stability when we included the U-correction in our calculations. Its structure (Fig. 3g) has space group $Cmmm$. For both $U - J$ = 1 and $U - J$ = 2, this phase has an easy axis anisotropy with a large anisotropy field and a rather high MAE, but small spontaneous magnetization makes the energy product to be the lowest among all studied phases.

Our results show that systems containing Mn have large MAE, perhaps the heavy element can enhance spin-orbit coupling at Mn sites for this crystal symmetries. MAE curve for each selected materials is shown in Fig. 4 and calculated magnetic properties are collected in Table 2 and can be compared with modern rare earth hard magnets. Lattice parameters of selected compounds and available experimental values are provided in Table 3. Also, ($U - J$)-composition phase diagrams of the Fe-Sn, Mn-Sn and W-Mn-B systems and details of crystal structure and magnetic moments are collected in Supplementary

Table 2: Properties of our predicted compounds, compared with modern permanent magnets obtained experimentally($FePt$, Sm_2Co_{17}, $Nd_2Fe_{14}B$ and $Sm_2Fe_{17}N_3$)[85].

Compound	**space group**	$(U-J)$ (eV)	$\mathbf{M}_0$ (MA/m)	$\lvert\mathbf{K}_1\rvert$ (MJ/m^3)	$\lvert\mathbf{K}_2\rvert$ (MJ/m^3)	**MAE** (MJ/m^3)	κ	$\mathbf{H}_a$ (T)	$\lvert\mathbf{BH}\rvert_{\mathrm{MAX}}$ $(KJ.m^{-3})$	**easy axis/plane**
	$Pmm2$	0	0.25	2.76	—	2.76	5.92	22.0	19.7	—
W_3MnB_4	$Pmm2$	1	0.28	4.3	—	4.30	6.52	30.3	25.2	—
	$Pmm2$	2	0.32	5.70	—	5.70	6.63	35.5	32.4	—
$FeSn_2$	$I4/mcm$	0	0.257	1.89	0.0	1.89	4.76	16.7	20.7	easy plane
Fe_3Sn	$P6_3/mmc$	0	1.15	1.08	0.0	1.08	0.80	1.87	416	easy plane
	$P6_3/mmc$	2	1.32	0.16	0	0.16	0.27	0.23	545	easy axis
	$P6/mmm$	0	0.58	0.73	0.2	0.86	1.44	3.00	105	easy axis
$MnSn$	$P6/mmm$	1	0.72	0.67	0.10	0.65	1.00	1.81	164	easy plane
	$P6/mmm$	2	0.78	0.79	0.01	0.86	1.06	2.2	192	easy plane
$MnSn_4$	$Cmmm$	1	0.23	1.20	0.01	1.19	4.18	10.2	17.1	easy axis
	$Cmmm$	2	0.25	0.91	0.04	0.96	3.47	7.60	19.9	easy axis
$FePt$		0	1.09	13.8	0.31	14.1	3.06	25.8	375	easy axis
		1	1.14	11.5	0.20	11.7	2.7	20.6	407	easy axis
		4	1.2	8.85	0.04	8.89	2.24	15	443	easy axis
experimental										
$FePt$		-	1.14	6.6	-	-	2.00	28.9	406	-
Sm_2Co_{17}		-	0.97	4.2	-	-	1.87	21.5	294	-
$Nd_2Fe_{14}B$		-	1.28	4.9	-	-	1.54	19	512	-
$Sm_2Fe_{17}N_3$		-	1.233	8.6	-	-	2.13	35	473	-
$SmCo_5$		-	0.88	17.2	-	-	4.33	39.1	231	-

Table 3: DFT energies of formation, space groups and optimized lattice parameters from our calculations and available experiments (Full information about structural properties and energies is in the Supplementary Information).

Compound	**space group**	$(U-J)$(eV)	**Lattice parameters for selected** $(U-J)$					**ΔH**
		range of stability	a(Å)	b (Å)	c (Å)	$\beta_{(\text{degree})}$	$(U-J)$ (eV)	(eV/atom)
W_2MnB_2	$Immm$	$0.0 \leq U-J < 0.3$	3.120	4.668	7.200	-	0	-0.492
W_2MnB_2	P_4/mbm	$0.3 \leq U-J$	5.812	5.812	3.176	-	1	-0.522
W_2MnB_2	P_4/mbm		5.786	5.786	3.160	-	EXP[70]	
W_3MnB_4	$Pmm2$	—	3.145	3.070	8.289	-	0	-0.484
W_3MnB_4	$Pmm2$	—	3.159	3.076	8.329	-	1	-0.510
W_3MnB_4	$Pmm2$	—	3.158	3.076	8.329	-	2	-0.468
$WMnB_2$	$I\bar{4}m2$	$0.0 \leq U-J \leq 0.9$	3.069	3.069	16.063	-	0	-0.538
$WMnB_2$	$Pmmn$	$0.9 < U-J \leq 1.6$	3.047	3.104	7.979	-	1	-0.566
$WMnB_2$	$Amm2$	$1.6 < U-J$	3.017	3.104	8.128	-	2	-0.449
$WMnB_2$	$Amm2$		3.012	3.120	8.130	-	[EXP, this work]	
$W_2Mn_3B_2$	$A2/m$	$0.0 \leq U-J < 0.9$	8.645	2.940	6.296	112	0	-0.412
$W_2Mn_3B_2$	$A2/m$	$0.9 \leq U-J < 1.5$	8.513	3.136	5.767	81	1	-0.425
$FeSn_2$	$I4/mcm$	$0.0 \leq U-J \leq 0.4$	6.559	6.559	5.326	-	0	-0.0065
$FeSn_2$	$I4/mcm$		6.533	6.533	5.323	-	EXP[86]	
Fe_3Sn	$P6_3/mmc$	$1.7 < U-J$	5.522	5.522	4.344	-	2	-0.0159
Fe_3Sn	$P6_3/mmc$		5.464	5.464	4.352	-	EXP[87]	
Fe_3Sn_2	$R\bar{3}m$	$0.0 \leq U-J \leq 1.7$	5.326	5.326	19.803	-	0	-0.0174
Fe_3Sn_2	$R\bar{3}m$		5.344	5.344	19.797	-	EXP[79]	
$MnSn$	$P6/mmm$	—	5.389	5.389	4.478	-	0	-0.0560
$MnSn$	$P6/mmm$	—	5.411	5.411	4.546	-	1	-0.0925
$MnSn$	$P6/mmm$	—	5.680	5.680	4.780	-	2	-0.0775
$MnSn_4$	$Cmmm$	$0.7 \leq U-J$	12.678	6.422	3.131	-	1	-0.0423
$MnSn_4$	$Cmmm$		12.763	6.502	3.156	-	2	-0.0507
$MnSn_2$	$I4/mcm$	$0.6 \leq U-J$	6.725	6.725	5.528	-	1	-0.067
$MnSn_2$	$I4/mcm$		6.671	6.671	5.443	-	EXP[88]	

Information.

4 CONCLUSIONS

Magnetic materials are challenging for several reasons. First, multiple magnetic structures are very close in energy and cannot be exhaustively sampled in many cases. Second, standard DFT calculations are often too crude, and DFT+U is only semiquantitative. Here, we show how a simple extension of the evolutionary algorithm USPEX allowed us to optimize the magnetic structure together with atomic structure and chemical composition. Detailed DFT+DMFT calculations and experiments can then be performed for the most interesting predicted materials. A new function for quantifying half-metallicity of a material is proposed and several low-energy half-metal phases are predicted in the Cr-O system using multi-objective Pareto optimization as implemented in evolutionary algorithm USPEX. Using USPEX, we searched for stable phases with high magnetization Thereafter promising predicted system were studied more thoroughly. Our aim is to discover materials with high energy product $|BH|_{\mathrm{MAX}}$ as well as high anisotropy field H_a. For example, our results shows high value of $|BH|_{\mathrm{MAX}}$ for Fe_3Sn and MnSn(due to a high magnetization M_0), and high anisotropy field in Mn-rich phases. In the studied systems (i.e. W-Mn-B, Fe-Sn and Mn-Sn), our calculations recovered all experimentally known compounds and crystal structures, and resulted in a number of new predictions, also checking if larger cell magnetic ordering exists. One of the newly predicted materials, antiferromagnetic $WMnB_2$ has been confirmed by direct experimental synthesis.

In total we predicted five magnetic materials in our USPEX-calculations. Two of them, Fe_3Sn and MnSn, theoretically, have shown high $|BH|_{\mathrm{MAX}}$ and rather high anisotropy field, which is comparable to available hard magnets, and exceed or comparable to other theoretically predicted compounds with no rare-earth elements [89–91], thus they are of potential technological interest. W_3MnB_4 has also shown high anisotropy field, but its relatively low energy product is a drawback. In short, we can say that our method has shown great power, and the goal of finding rare earth-free hard magnets appears achievable.

The main current limitation is the imperfect description of such systems by both DFT and DFT+U. Exploring ranges of $(U - J)$ values and building "correlation phase diagram" gives a range of possible solutions (see the Supplementary Information). There is an ongoing debate as to how to model electron correlations in magnetic materials in order to obtain reliable results cheaply. Even within the DFT+U approach, recent studies have shown that varying U and J separately are more reliable than only using their difference [92]. Irrespective of which way of modeling electron correlations is better, our work describes the framework which can be used in conjunction with any method for calculating magnetic properties, and as the accuracy of such methods improves, the prediction of novel magnetic materials within our approach will become more and more accessible.

Data Availability

The data that support the findings of this study are available from the corresponding author upon reasonable request.

Code Availability

The extension of USPEX to magnetic materials are publicly available. The extension of USPEX to half-metals will be available in the next releases.

Acknowledgments

Theoretical studies of ferromagnets and DFT+DMFT calculations were supported by Russian Science Foundation (grant 19-72-30043). We thank Dr. V.A. Mukhanov for assistance in high-pressure experiments, and I.V. Blinov, P. Yu. Plechov, and A.N. Vasilyev for their help in the beginning of this project.

Author Contribution

G.R.Q. made the first implementation of the extension of USPEX to magnetic materials. S.R. and A.R.O. created the half-metallicity fitness function and Z.A. Implemented it. S.R. and Z.A. searched for promising candidates and performed calculations on permanent magnets and half-metals. V.L.S. performed the high-pressure synthesis of $WMnB_2$, and contributed to writing the paper. I.B.P., K.V.M., A.S.M., A.V.Ch., A.V.K.,and N.V.M. performed synthesis and measurement of properties of $WMnB_2$ at ambient pressure, and contributed to writing the paper. E.V.T. checked the Curie temperatures. A.S.B., A.A.K., and V.I.A. did DFT+DMFT calculations on $WMnB_2$ and Fe_3Sn, and contributed to writing the paper. H.L. calculated the DOS and bandstructures of the Cr-O candidates. S.R., Z.A., and A.R.O. wrote the paper.

Competing Interests

The authors declare no competing interests.

References and Notes

[1] Strnat, K. The recent development of permanent magnet materials containing rare earth metals. *IEEE Transactions on Magnetics* **6**, 182–190 (1970).

[2] Bader, S. & Parkin, S. Spintronics. *Annual Review of Condensed Matter Physics* **1**, 71–88 (2010).

[3] Wolf, S. A., Chtchelkanova, A. Y. & Treger, D. M. Spintronic – a retrospective and perspective. *IBM Journal of Research and Development* **50**, 101–110 (2006).

[4] Coey, J. M. D. Hard magnetic materials: A perspective. *IEEE Transactions on Magnetics* **47**, 4671–4681 (2011).

[5] Oganov, A. R. *et al. Computational materials discovery* (Royal Society of Chemistry, 2018).

[6] Oganov, A. R., Pickard, C. J., Zhu, Q. & Needs, R. J. Structure prediction drives materials discovery. *Nature Reviews Materials* **4**, 331–348 (2019).

[7] Curtarolo, S. *et al.* The high-throughput highway to computational materials design. *Nature materials* **12**, 191–201 (2013).

[8] Oganov, A. R. & Glass, C. W. Crystal structure prediction using ab initio evolutionary techniques: Principles and applications. *The Journal of chemical physics* **124**, 244704 (2006).

[9] Lyakhov, A. O., Oganov, A. R., Stokes, H. T. & Zhu, Q. New developments in evolutionary structure prediction algorithm USPEX. *Computer Physics Communications* **184**, 1172–1182 (2013).

[10] Allahyari, Z. & Oganov, A. R. Coevolutionary search for optimal materials in the space of all possible compounds. *npj Computational Materials* **6**, 1–10 (2020).

[11] Zhao, X. *et al.* Exploring the structural complexity of intermetallic compounds by an adaptive genetic algorithm. *Phys. Rev. Lett.* **112**, 045502 (2014).

[12] Halder, A., Nafday, D., Sanyal, P. & Saha-Dasgupta, T. Computer predictions on rh-based double perovskites with unusual electronic and magnetic properties. *npj Quantum Materials* **3**, 1–8 (2018).

[13] Oganov, A. R., Ma, Y., Lyakhov, A. O., Valle, M. & Gatti, C. Evolutionary Crystal Structure Prediction as a Method for the Discovery of Minerals and Materials. *Reviews in Mineralogy and Geochemistry* **71**, 271–298 (2010).

[14] Oganov, A. R., Lyakhov, A. O. & Valle, M. How evolutionary crystal structure prediction works and why. *Accounts of Chemical Research* **44**, 227–237 (2011). PMID: 21361336.

[15] Perdew, J. P., Burke, K. & Ernzerhof, M. Generalized gradient approximation made simple. *Phys. Rev. Lett.* **77**, 3865–3868 (1996).

[16] Liechtenstein, A. I., Anisimov, V. I. & Zaanen, J. Density-functional theory and strong interactions: Orbital ordering in mott-hubbard insulators. *Phys. Rev. B* **52**, R5467–R5470 (1995).

[17] Dudarev, S. L., Botton, G. A., Savrasov, S. Y., Humphreys, C. J. & Sutton, A. P. Electron-energy-loss spectra and the structural stability of nickel oxide: An LSDA+U study. *Phys. Rev. B* **57**, 1505–1509 (1998).

[18] Kvashnin, A. G., Oganov, A. R., Samtsevich, A. I. & Allahyari, Z. Computational search for novel hard chromium-based materials. *The Journal of Physical Chemistry Letters* **8**, 755–764 (2017). PMID: 28103665.

[19] Zhu, Q., Li, L., Oganov, A. R. & Allen, P. B. Evolutionary method for predicting surface reconstructions with variable stoichiometry. *Phys. Rev. B* **87**, 195317 (2013).

[20] Sharma, V. *et al.* Rational design of all organic polymer dielectrics. *Nature communications* **5**, 1–8 (2014).

[21] Hu, C. H. *et al.* Pressure-induced stabilization and insulator-superconductor transition of BH. *Phys. Rev. Lett.* **110**, 165504 (2013).

[22] Zhang, W. *et al.* Unexpected stable stoichiometries of sodium chlorides. *Science* **342**, 1502–1505 (2013).

[23] Zhou, X. F., Oganov, A. R., Qian, G.-R. & Zhu, Q. First-principles determination of the structure of magnesium borohydride. *Phys. Rev. Lett.* **109**, 245503 (2012).

[24] Qian, G.-R., Lyakhov, A. O., Zhu, Q., Oganov, A. R. & Dong, X. Novel hydrogen hydrate structures under pressure. *Scientific reports* **4**, 5606 (2014).

[25] Kresse, G. & Hafner, J. Ab initio molecular dynamics for liquid metals. *Phys. Rev. B* **47**, 558–561 (1993).

[26] Kresse, G. & Hafner, J. Ab initio molecular-dynamics simulation of the liquid-metal–amorphous-semiconductor transition in germanium. *Phys. Rev. B* **49**, 14251–14269 (1994).

[27] Kresse, G. & Furthmuller, J. Efficiency of ab-initio total energy calculations for metals and semiconductors using a plane-wave basis set. *Computational Materials Science* **6**, 15 – 50 (1996).

[28] Kresse, G. & Furthmüller, J. Efficient iterative schemes for ab initio total-energy calculations using a plane-wave basis set. *Phys. Rev. B* **54**, 11169–11186 (1996).

[29] Anisimov, V. I., Zaanen, J. & Andersen, O. K. Band theory and mott insulators: Hubbard u instead of stoner i. *Phys. Rev. B* **44**, 943–954 (1991).

[30] Anisimov, V. I., Solovyev, I. V., Korotin, M. A., Czyżyk, M. T. & Sawatzky, G. A. Density-functional theory and nio photoemission spectra. *Phys. Rev. B* **48**, 16929–16934 (1993).

[31] Solovyev, I. V., Dederichs, P. H. & Anisimov, V. I. Corrected atomic limit in the local-density approximation and the electronic structure of d impurities in rb. *Phys. Rev. B* **50**, 16861–16871 (1994).

[32] Himmetoglu, B., Floris, A., de Gironcoli, S. & Cococcioni, M. Hubbard-corrected dft energy functionals: The lda+u description of correlated systems. *International Journal of Quantum Chemistry* **114**, 14–49 (2014).

[33] Metzner, W. & Vollhardt, D. Correlated lattice fermions in $d = \infty$ dimensions. *Phys. Rev. Lett.* **62**, 324–327 (1989).

[34] Georges, A., Kotliar, G., Krauth, W. & Rozenberg, M. J. Dynamical mean-field theory of strongly correlated fermion systems and the limit of infinite dimensions. *Rev. Mod. Phys.* **68**, 13–125 (1996).

[35] Anisimov, V. I., Poteryaev, A. I., Korotin, M. A., Anokhin, A. O. & Kotliar, G. First-principles

calculations of the electronic structure and spectra of strongly correlated systems: dynamical mean-field theory. *Journal of Physics: Condensed Matter* **9**, 7359–7367 (1997).

[36] Kotliar, G. *et al.* Electronic structure calculations with dynamical mean-field theory. *Rev. Mod. Phys.* **78**, 865–951 (2006).

[37] Anisimov, V. & Izyumov, Y. In *Electronic Structure of Strongly Correlated Materials* (Springer, 2010).

[38] Advanced materials simulation ekaterinburg's toolbox(amulet).

[39] Anisimov, V. I., Aryasetiawan, F. & Lichtenstein, A. I. First-principles calculations of the electronic structure and spectra of strongly correlated systems: the LDA+u method. *Journal of Physics: Condensed Matter* **9**, 767–808 (1997).

[40] Krukau, A. V., Vydrov, O. A., Izmaylov, A. F. & Scuseria, G. E. Influence of the exchange screening parameter on the performance of screened hybrid functionals. *The Journal of Chemical Physics* **125**, 224106 (2006).

[41] Heyd, J., Scuseria, G. E. & Ernzerhof, M. Hybrid functionals based on a screened coulomb potential. *The Journal of Chemical Physics* **118**, 8207–8215 (2003).

[42] Jia, W. *et al.* The analysis of a plane wave pseudopotential density functional theory code on a GPU machine. *Computer Physics Communications* **184**, 9 – 18 (2013).

[43] Jia, W. *et al.* Fast plane wave density functional theory molecular dynamics calculations on multi-GPU machines. *Journal of Computational Physics* **251**, 102 – 115 (2013).

[44] Harris, J. Simplified method for calculating the energy of weakly interacting fragments. *Phys. Rev. B* **31**, 1770–1779 (1985).

[45] Skomski, R. *et al. Simple models of magnetism* (Oxford University Press on Demand, 2008).

[46] Coey, J. M. D. & Sanvito, S. Magnetic semiconductors and half-metals. *Journal of Physics D: Applied Physics* **37**, 988–993 (2004).

[47] Shan, R. *et al.* Demonstration of half-metallicity in fermi-level-tuned heusler alloy $Co_2FeAl_{0.5}Si_{0.5}$ at room temperature. *Phys. Rev. Lett.* **102**, 246601 (2009).

[48] Katsnelson, M. I., Irkhin, V. Y., Chioncel, L., Lichtenstein, A. I. & de Groot, R. A. Half-metallic ferromagnets: From band structure to many-body effects. *Rev. Mod. Phys.* **80**, 315–378 (2008).

[49] de Groot, R. A., Mueller, F. M., Engen, P. G. v. & Buschow, K. H. J. New class of materials: Half-metallic ferromagnets. *Phys. Rev. Lett.* **50**, 2024–2027 (1983).

[50] Halder, A., Ghosh, A. & Dasgupta, T. S. Machine-learning-assisted prediction of magnetic double perovskites. *Phys. Rev. Materials* **3**, 084418 (2019).

[51] Sanvito, S. *et al.* Accelerated discovery of new magnets in the heusler alloy family. *Science Advances* **3** (2017).

[52] Tang, C., Zhang, C., Jiang, Z., Ostrikov, K. & Du, A. Theoretical discovery of dirac half metal in experimentally synthesized two dimensional metal semiquinoid frameworks. *Journal of Materials Chemistry C* **7**, 5792–5796 (2019).

[53] Lu, S. *et al.* Coupling a crystal graph multilayer descriptor to active learning for rapid discovery of 2D ferromagnetic semiconductors/half-metals/metals. *Advanced Materials* **32**, 2002658 (2020).

[54] Griffin, S. M. & Neaton, J. B. Prediction of a new class of half-metallic ferromagnets from first principles. *Phys. Rev. Materials* **1**, 044401 (2017).

[55] Kandpal, H. C., Fecher, G. H. & Felser, C. Calculated electronic and magnetic properties of the half-metallic, transition metal based heusler compounds. *Journal of Physics D: Applied Physics* **40**, 1507–1523 (2007).

[56] Allahyari, Z. & Oganov, A. R. *Multi-objective Optimization as a Tool for Material Design*, 2777–2790 (Springer International Publishing, Cham, 2020).

[57] Nunez-Valdez, M., Allahyari, Z., Fan, T. & Oganov, A. R. Efficient technique for computational design of thermoelectric materials. *Computer Physics Communications* **222**, 152 – 157 (2018).

[58] Sims, H., Oset, S. J., Butler, W. H., MacLaren, J. M. & Marsman, M. Determining the anisotropic exchange coupling of cro_2 via first-principles density functional theory calculations. *Phys. Rev. B* **81**, 224436 (2010).

[59] Materials Project.

[60] Wang, L., Maxisch, T. & Ceder, G. Oxidation energies of transition metal oxides within the GGA+U framework. *Phys. Rev. B* **73**, 195107 (2006).

[61] Jain, A. *et al.* Commentary: The materials project: A materials genome approach to accelerating materials innovation. *APL Materials* **1**, 011002 (2013).

[62] Maldonado, F., Rivera, R. & Stashans, A. Structure, electronic and magnetic properties of ca-doped chromium oxide studied by the dft method. *Physica B: Condensed Matter* **407**, 1262 – 1267 (2012).

[63] Cloud, W. H., Schreiber, D. S. & Babcock, K. R. X-ray and magnetic studies of cro2 single crystals. *Journal of Applied Physics* **33**, 1193–1194 (1962).

[64] Singh, G. P., Ram, S., Eckert, J. & Fecht, H.-J. Synthesis and morphological stability in CrO2single crystals of a half-metallic ferromagnetic compound. *Journal of Physics: Conference Series* **144**, 012110 (2009).

[65] Dho, J., Ki, S., Gubkin, A., Park, J. & Sherstobitova, E. A neutron diffraction study of half-metallic ferromagnet CrO_2 nanorods. *Solid State Communications* **150**, 86 – 90 (2010).

[66] Haynes, W. M. *CRC handbook of chemistry and physics* (CRC press, 2014).

[67] Hill, A. H., Harrison, A., Dickinson, C., Zhou, W. & Kockelmann, W. Crystallographic and magnetic studies of mesoporous eskolaite, Cr_2O_3. *Microporous and Mesoporous Materials* **130**, 280 – 286 (2010).

[68] Allison, T. JANAF thermochemical tables, NIST standard reference database 13 (1996).

[69] Telegus, V. & Kuz'ma, Y. B. Ternary phases with the structure of the u_3si_2 type in the W–Mn–B and Mo–Mn–B systems. Tech. Rep., Lvov State Univ. (1968).

[70] Telegus, V. & Kuz'ma, Y. B. Phase equilibria in the systems vanadium-manganese-boron, molybdenum-manganese-boron, and tungsten-manganese-bor on. *Soviet Powder Metallurgy and Metal Ceramics* **10**, 52–56 (1971).

[71] Skomski, R. & Coey, J. M. D. Giant energy product in nanostructured two-phase magnets. *Phys. Rev. B* **48**, 15812–15816 (1993).

[72] Kneller, E. & Hawig, R. The exchange-spring magnet: a new material principle for permanent magnets. *IEEE Transactions on Magnetics* **27**, 3588–3560 (1991).

[73] Since we have a structure with a large unit cell, doing antiferromagnetic calculation would require a supercell of 8 times larger than the unit cell, so practically doing such DFT+U calculation for nearly a hundred atoms in a supercell is impossible.

[74] Biermann, S. *et al.* Observation of hubbard bands in γ-manganese. *Journal of Experimental and Theoretical Physics Letters* **80**, 612–615 (2004).

[75] Di Marco, I. *et al.* Correlation effects in the total energy, the bulk modulus, and the lattice constant of a transition metal: Combined local-density approximation and dynamical mean-field theory applied to Ni and Mn. *Phys. Rev. B* **79**, 115111 (2009).

[76] Korotin, D. *et al.* Construction and solution of a wannier-functions based hamiltonian in the pseudopotential plane-wave framework for strongly correlated materials. *Eur. Phys. J. B* **65**, 91–98 (2008).

[77] Telegus, V. Reaction of groups VI and VII transition metals with boron (1970).

[78] Le Bail, A., Duroy, H. & Fourquet, J. Ab-initio structure determination of lisbwo6 by X-ray powder diffraction. *Materials Research Bulletin* **23**, 447 – 452 (1988).

[79] Giefers, H. & Nicol, M. High pressure X-ray diffraction study of all Fe-Sn intermetallic compounds and one Fe-Sn solid solution. *Journal of Alloys and Compounds* **422**, 132 – 144 (2006).

[80] Fayyazi, B. *et al.* Experimental and computational analysis of binary Fe-Sn ferromagnetic compounds. *Acta Materialia* **180**, 126–140 (2019).

[81] Sales, B. C., Saparov, B., McGuire, M. A., Singh, D. J. & Parker, D. S. Ferromagnetism of Fe_3Sn and alloys. *Scientific reports* **4**, 1–6 (2014).

[82] Belozerov, A. S. & Anisimov, V. I. Coulomb interaction parameters in bcc iron: an LDA+DMFT study. *Journal of Physics: Condensed Matter* **26**, 375601 (2014).

[83] Antipov, A. E., Krivenko, I. S., Anisimov, V. I., Lichtenstein, A. I. & Rubtsov, A. N. Role of rotational symmetry in the magnetism of a multiorbital model. *Phys. Rev. B* **86**, 155107 (2012).

[84] Hausoel, A. *et al.* Local magnetic moments in iron and nickel at ambient and earth's core conditions. *Nature communications* **8**, 1–9 (2017).

[85] Coey, J. M. *Magnetism and magnetic materials* (Cambridge university press, 2010).

[86] Armbruster, M., Schmidt, M., Cardoso-Gil, R., Borrmann, H. & Grin, Y. Crystal structures of iron distannide, $FeSn_2$, and cobalt distannide, $CoSn_2$. *Zeitschrift fur Kristallographie - New Crystal Structures* **222**, 83 – 84 (2007).

[87] Echevarria-Bonet, C. *et al.* Structural and magnetic properties of hexagonal Fe_3Sn prepared by non-equilibrium techniques. *Journal of Alloys and Compounds* **769**, 843 – 847 (2018).

[88] Armbruster, M., Schnelle, W., Cardoso-Gil, R. & Grin, Y. Chemical bonding in compounds of the $CuAl_2$ family: $MnSn_2$, $FeSn_2$ and $CoSn_2$. *Chemistry - A European Journal* **16**, 10357–10365 (2010).

[89] Flores-Livas, J. A. Crystal structure prediction of magnetic materials. *Journal of Physics: Condensed Matter* **32**, 294002 (2020).

[90] Zhang, Y., Miller, G. J. & Fokwa, B. P. T. Computational design of rare-earth-free magnets with the $Ti_3Co_5B_2$-type structure. *Chemistry of Materials* **29**, 2535–2541 (2017).

[91] Vishina, A. *et al.* High-throughput and data-mining approach to predict new rare-earth free permanent magnets. *Phys. Rev. B* **101**, 094407 (2020).

[92] Linscott, E. B., Cole, D. J., Payne, M. C. & O'Regan, D. D. Role of spin in the calculation of hubbard U and hund's J parameters from first principles. *Phys. Rev. B* **98**, 235157 (2018).